ACS APPLIED MATERIALS & INTERFACES

Research Article

www.acsami.org

Visible-Light-Active Plasmonic Ag–$SrTiO_3$ Nanocomposites for the Degradation of NO in Air with High Selectivity

Qian Zhang,[†] Yu Huang,*[,†,‡] Lifeng Xu,[†] Jun-ji Cao,*[,†,‡] Wingkei Ho,[§] and Shun Cheng Lee[∥]

[†]Key Laboratory of Aerosol Chemistry and Physics, Institute of Earth Environment, Chinese Academy of Sciences, Xi'an 710061, China

[‡]State Key Lab of Loess and Quaternary Geology (SKLLQG), Institute of Earth Environment, Chinese Academy of Sciences, Xi'an 710061, China

[§]Department of Science and Environmental Studies, The Hong Kong Institute of Education, Hong Kong, China

[∥]Department of Civil and Environmental Engineering, The Hong Kong Polytechnic University, Hung Hom, Hong Kong, China

Supporting Information

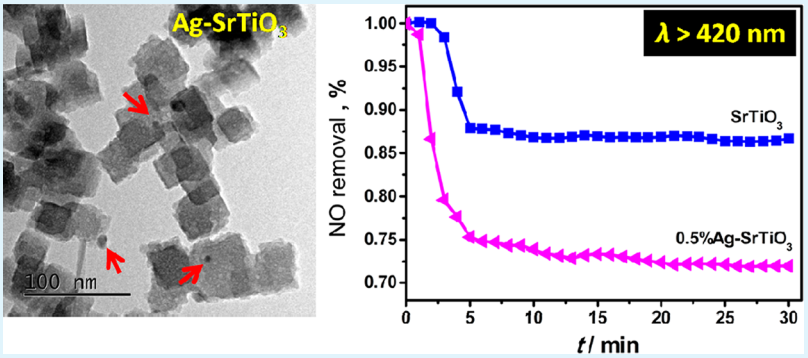

ABSTRACT: Harnessing inexhaustible solar energy for photocatalytic disposal of nitrogen oxides is of great significance nowadays. In this study, Ag–$SrTiO_3$ nanocomposites (Ag–STO) were synthesized via one-pot solvothermal method for the first time. The deposition of Ag nanoparticles incurs a broad plasmonic resonance absorption in the visible light range, resulting in enhanced visible light driven activity on NO removal in comparison with pristine $SrTiO_3$. The Ag loading amount has a significant influence on light absorption properties of Ag–STO, which further affects the photocatalytic efficiency. It was shown that 0.5% Ag loading onto $SrTiO_3$ (in mass ratio) could remove 30% of NO in a single reaction path under visible light irradiation, which is twice higher than that achieved on pristine $SrTiO_3$. Most importantly, the generation of harmful intermediate (NO_2) is largely inhibited over $SrTiO_3$ and Ag–STO nanocomposites, which can be ascribed to the basic surface property of strontium sites. As identified by electron spin resonance (ESR) spectra,·O_2^- and ·OH radicals are the major reactive species for NO oxidation. Essentially speaking, the abundance of reactive oxygen radicals produced over Ag–STO nanocomposites are responsible for the improved photocatalytic activity. This work provides a facile and controllable route to fabricate plasmonic Ag–$SrTiO_3$ nanocomposite photocatalyst featuring high visible light activity and selectivity for NO abatement.

KEYWORDS: *air pollution control, Ag–$SrTiO_3$ nanocomposites, plasmonic effect, photocatalysis, NO removal*

1. INTRODUCTION

A close correlation between haze events and secondary aerosol formation in China has been pointed out recently by a *Nature* report.[1] It was suggested that reducing the emission of secondary aerosol precursors, namely nitrogen oxides (NO_x, mainly referring to NO and NO_2) and volatile organic compounds (VOCs), is important for mitigating the air pollution problems.[2] Fossil fuel combustion is a great contributor to the emission of nitrogen oxides, from diverse sources ranging from thermal power plants to mobile vehicles. Targeting for NO_x emitted from these sources at high concentration, deNO_x techniques like selective catalytic reduction (SCR) and three-way catalysis (TWC), have been developed and considerable progress has been made over the past decades.[3,4] However, the above-mentioned strategies are not technically feasible to treat ambient air pollutants. As the accumulation of gaseous pollutants continues, it becomes more urgent to remove NO_x from the ambient conditions.

Photocatalysis has been considered as a promising technology for decomposing low concentration pollutants in the environment, since the photodegradation of polychlorinated biphenyl conducted by Carey in 1976.[5,6] On one hand, considerable work related with the synthesis of efficient photocatalysts for NO_x removal, such as Fe_2O_3,[7] Mn^{4+}-doped

Received: December 7, 2015
Accepted: January 21, 2016
Published: January 21, 2016

DOI: 10.1021/acsami.5b11887
ACS Appl. Mater. Interfaces 2016, 8, 4165–4174

anatase,[8] BiOBr[9,10] and g-C_3N_4,[11,12] and the mechanism analysis were conducted.[13−20] On the other hand, the field tests employing photocatalysis to reduce atmospheric NO_x level in busy streets and tunnels were carried out.[21−23] These studies provided encouraging results for the development and commercial application of photocatalysis in air purification in the near future.

Perovskite oxides, with the general formula of ABO_3 (or A_2BO_4), are important functional materials for heterogeneous catalysis, due to the flexible chemical composition, element abundance and structural stability.[24] Perovskites are widely studied as catalysts for SCR processes,[25,26] whereas the potential ability as photocatalysts for NO_x abatement is rarely focused. As an important *n*-type perovskite semiconductor, strontium titanate ($SrTiO_3$) has attracted lots of attention in solar H_2 production and energy conversion applications over the past years.[27−32] One of the great advantages of $SrTiO_3$, in comparison with TiO_2, is the higher conduction band position (−1.4 V vs SCE at pH 13) that drives more efficient charge transfer to electron acceptor (e.g., O_2), leading to enhanced photocatalytic efficiencies.[33,34] Moreover, it is expected that with the presence of strontium sites, the interaction between NO molecule and the photocatalyst would change, possibly promoting the complete conversion of NO.[35] Nevertheless, $SrTiO_3$ can only be excited by light with shorter wavelength, owing to its wide band gap energy of 3.2 eV. To endow $SrTiO_3$ with visible light harvesting property, substitutional doping is normally adopted due to the excellent tolerance of perovskite structure.[36−39] Although effective bandgap narrowing can be achieved, due to the hard control over the generation of continuous midgap states, charge recombination is inevitably encountered.

Recently, plasmonic nanostructures have drawn a great deal of attention in the field of photocatalysis for the merit of intense light absorption. Previous studies proved that coupling plasmonic nanostructures (namely Au and Ag nanoparticles) with wide bandgap semiconductors, is able to extend the light absorption into visible range and achieve higher photocatalytic rates.[40] For example, R. Saravanan synthesized ternary ZnO/Ag/CdO nanocomposite and showed that this material exhibited pronounced activity for industrial textile removal under visible light.[41] Essentially speaking, the electrons on the surface of plasmonic nanostructure can be strongly interacted with incoming photons when their oscillating frequencies are matched, and give rise to the so-called localized surface plasmon resonance (LSPR).[42] This physical property is usually characterized by a strong light absorption at certain wavelengths, which varies with different metals, sizes and shapes.[43] Though it still remains ambiguous, the mechanism for plasmonic improved photocatalysis is mainly categorized into charge transfer and local electric field enhancement.[44−47] There are several methods available for depositing plasmonic nanostructures onto semiconductor surface, for example, Y. He and co-workers employed the oblique angle codeposition method to embed Ag nanoparticles with TiO_2 nanorods;[48] D. Ding et al. used the ligand exchange approach to construct Au/TiO_2 photocatalysts with well controlled sizes and SPR properties.[49] However, these methods often require tedious procedures that are not economically feasible.

Herein, we propose the one-pot fabrication of plasmonic Ag−$SrTiO_3$ nanocomposites toward photocatalytic elimination of NO. The loading amount of Ag nanoparticles could be easily tuned by changing the concentration of precursor $AgNO_3$. Comprehensive characterizations of materials were conducted, and the photocatalytic mechanism of Ag−$SrTiO_3$ nanocomposites for NO removal was proposed. To the best of our knowledge, this is the first time to prepare Ag−$SrTiO_3$ nanocomposites in a one-pot process, and a series of Ag−$SrTiO_3$ composites with differing weight ratios were evaluated for their photocatalytic performances.

2. EXPERIMENTAL SECTION

2.1. Preparation of Pristine $SrTiO_3$, Ag−$SrTiO_3$, and Pure Ag Samples. All chemicals used throughout the experiments were of analytical grade purchased from Sigma-Aldrich without further purification. Ag−$SrTiO_3$ (Ag−STO) samples were prepared by the one-pot solvothermal method. Typically, 5 mL of $Sr(NO_3)_2$ aqueous solution was slowly added into 30 mL of titanium tetraisopropoxide (TTIP)−ethanol solution at equal mole and agitated for 30 min, to which 0.2 mol L^{-1} mineralizing agent NaOH was added and stirred for another 30 min. $AgNO_3$ precursors with different amount were introduced into the above solution, respectively. The mixture was transferred into a 50 mL Teflon-lined stainless steel autoclave and kept at 160 °C for 24 h. The obtained Ag−STO products were rinsed, dried and finally annealed in Ar at 350 °C for 30 min to ensure the intimate contact between Ag and STO.

For comparison, pristine $SrTiO_3$ was prepared with the same method except the addition of $AgNO_3$ solution. Metallic Ag was prepared by the same approach without introducing Sr and Ti precursors. For convenience, pristine $SrTiO_3$ sample were denoted as STO, and the Ag−$SrTiO_3$ nanocomposites with Ag weight ratios of 0.1%, 0.25%, 0.5% and 1% were denoted as 0.1% Ag−STO, 0.25% Ag−STO, 0.5% Ag−STO and 1% Ag−STO, respectively.

2.2. Characterization. The crystal structures of the samples were determined by the PANalytical X'pert Pro powder diffractometer at a scanning rate of 0.017° min^{-1} ranging from 20° to 80° (PANalytical Corp., The Netherlands). The morphology of the samples was characterized by SEM 6700F instrument (JEOL Corp., Japan), and TEM performed on the JEOL 2010 instrument at accelerating voltage of 100 kV (JEOL Corp., Japan), respectively. The surface chemical composition of Ag−STO nanocomposites was further analyzed by the X-ray photoelectron spectroscopy (Thermo Scientific, Escalab 250Xi, the United States), and the binding energies were calibrated by C 1s at 284.8 eV as a reference. The surface area of the samples was measured by the Gemini VII 3.03 instrument (Micromeritics Instrument Corp., the United States), with values obtained from the N_2 adsorption−desorption isotherms at 77 K in the partial pressure range of 0.05−0.35. The optical properties of the samples were investigated by the Agilent Cary 100 instrument (Agilent Corp., the United States) in the range of 200−800 nm, with Ba_2SO_4 reflection as a reference. To probe the formation of superoxide and hydroxyl radicals, electron spin resonance (ESR) measurements were conductedon a Bruker ER200-SRC instrument (Bruker Corp., Germany) at room temperature. LED lights at wavelength of 280 and 420 nm were used, respectively, during ESR studies. DMPO (5,5-dimethyl-l-pyrroline N-oxide) was used as the spin trapping agent, with deionized water and methanol as solvents, respectively, to detect the generation of hydroxyl radicals (DMPO−·OH) and superoxide radicals (DMPO−·O_2^-). The charge recombination kinetics of photocatalysts were studied by the photoluminescence spectra acquired from the F-7000 photoluminescence spectrometer (Hitachi, Japan) using excitation wavelength of 280 nm at room temperature. Fourier transform infrared (FT-IR) spectra of samples, before and after photocatalytic reactions were measured on the Bruker Vertex 70 spectrometer (Bruker Corp., Germany), using the KBr pellet method. Mott−Schottky plot of STO was measured in the three electrode configuration on Princeton Parstat 4000 potentiostat. For detailed information on electrode fabrication and measurement conditions, please see the Supporting Information.

2.3. Photocatalytic Activity Assessment. To assess the activity of STO and Ag−STO photocatalysts toward NO abatement in realistic conditions, the experiments were conducted in a continuous gas flow

DOI: 10.1021/acsami.5b11887
ACS Appl. Mater. Interfaces 2016, 8, 4165−4174

chamber designed according to a previous report.[50] The homemade stainless steel chamber is rectangular in shape with a top quartz glass panel, and the total volume of the chamber is 4.5 L. Inside the chamber, a round Petri dish containing 0.1 g of specimen was placed on the bottom, supported by a sample holder. The air/NO mixture at a concentration of 400 ppb was produced by diluting NO standard gas with zero air in the gas dilution calibrator (Sabio 4010, the United States), and accessed to the chamber through the inlet tube. The outlet tube was positioned at the same height on the opposite chamber wall, to allow the gas flow over the sample surface. The whole system was kept at room temperature. The light was provided by a 300 W electric input xenon lamp (Perfectlight, microsolar300, Beijing) positioned above the chamber, and the optical power density of visible light (420 nm cutoff filter) reaching the sample surface was 28.93 mW/cm^2 (calibrated by Thorlabs PM100D photometer). After the sample was placed in the chamber, the gas stream (at 3 L/min) was introduced to the chamber and stabilized for 30 min in the dark to achieve constant NO concentration. The xenon lamp was then switched on and the NO, NO_2 concentrations were continuously monitored. The removal ratio of NO at any given time was noted as C/C_0, where C is the NO concentration at any given time, ppb; and C_0 is the initial concentration of NO, ppb. NO_2 concentration was simultaneously recorded during the process, and the selectivity was calculated according to the following equation:[51]

$$NO_2 \text{ selectivity} = \frac{C_{NO_2}}{C_0 - C}$$

Where C_{NO_2} represents the production of NO_2, ppb; C_0 is the initial concentration of NO, ppb; and C is the final concentration of NO, ppb.

3. RESULTS AND DISCUSSION

3.1. XRD Characterizations and Surface Chemical States. Figure 1 shows the XRD patterns of synthesized

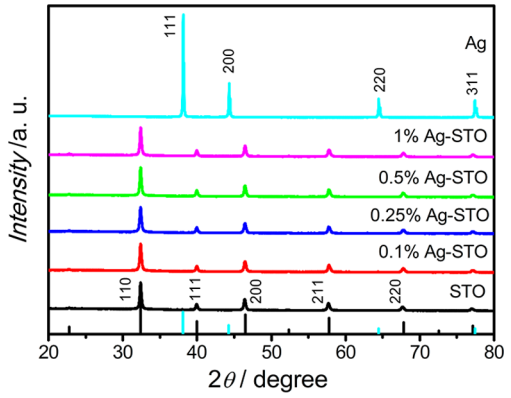

Figure 1. Powder XRD patterns of pure STO, pure Ag and Ag–STO nanocomposites with various Ag loading amount.

Ag–STO nanocomposites at various Ag loading amounts in comparison with those of pure STO and pure Ag nanoparticles. The peaks located at 32.4°, 39.9°, 46.5°, 57.8°, 67.8° and 77.2° can be well-indexed to the characteristic diffraction peaks of 110, 111, 200, 211, 220 and 310 planes of perovskite $SrTiO_3$ (JCPDS file No. 35-0734), suggesting that phase pure STO was formed and well crystallized with cubic structure.[52] The average particle size of STO is about 31.8 nm as estimated from the strongest 110 diffraction peak by Scherrer Equation.[53] Compared with pristine STO, major diffraction peaks belonging to STO were maintained for Ag–STO nanocomposites with similar fwhm (full width at half maxima) values, suggesting that the phase structure and crystallite size of STO were well preserved in addition of Ag precursor. Scrutinization of the dominant diffraction peak positions revealed no shift after Ag loading, excluding the possible doping of Ag^+ into $SrTiO_3$ crystal lattice. However, diffraction peaks belonging to Ag were not found in the pattern, which may be due to the low loading amount of Ag beyond the detection limit of the diffractometer. Characteristic peaks located at 38.1°, 44.3°, 64.4° and 77.5° justify the formation of cubic phase Ag (JCPDS file No. 04-0783) in the solvothermal environment.[54] Therefore, it was assumed that Ag nanoparticles were introduced onto the surface of STO at low amount by the one pot solvothermal approach.

To identify the surface chemical states and composition of the as-prepared Ag–STO samples, the 0.5% Ag–STO nanocomposite was characterized by X-ray photoelectronspectroscopy (XPS). Figure 2 presents the survey spectrum and high-resolution spectra of C 1s, Ag 3d, Sr 3d, Ti 3d and O 1s orbitals. The survey spectrum confirmed the presence of Sr, Ti, and O elements, whereas the peak for C 1s is ascribed to adventitious carbon during XPS measurement. The peak located at binding energy of 367.97 eV corresponds to the $3d_{5/2}$ orbital of Ag^0 species.[55] Quantitive analysis showed that the surface atomic percentage of Ag in STO was consistent with the precursor ratio, which demonstrates that all Ag precursors were transformed to Ag nanoparticles loaded on STO surface. In the spectrum of Sr 3d, the peaks at 132.85 and 134.37 eV correspond to Sr $3d_{5/2}$ and Sr $3d_{3/2}$, respectively, suggesting its existence as Sr^{2+} state. Titanium exists as the Ti^{4+} state was also verified by two separate peaks at 458.12 and 463.97 eV with a splitting orbital energy of 5.8 eV. Moreover, the asymmetric shape of O 1s peak, which can be deconvolved into two separate peaks centered at 529.51 and 530.87 eV, suggesting that titanium bonded oxygen (Ti–O) and hydrogen bonded oxygen (O–H) are both present on the surface.[56] The surface OH group, through reaction with photoinduced holes, would be potentially favorable for generation of ·OH radicals to catalyze NO oxidation reaction.

3.2. Morphological Structure. To understand the morphological and structural characteristics of the as-prepared STO and Ag–STO products, SEM and TEM characterizations were performed. Figure S1 shows the typical SEM images of STO and 0.5% Ag–STO nanocomposites, in which nanocubes with a size of ca. 40 nm can be seen. Figure 3a–d displays the typical TEM, high-resolution TEM (HRTEM) and SAED patterns of STO and Ag–STO samples. As presented in Figure 3a, strong contrast view in the image reveals that STO was formed in a square pattern, confirming the formation of STO nanocubes.[24] The dimension of STO was estimated to be around 35 nm from Figure 3a, which is consistent with the SEM and XRD calculation results. The high-resolution image in Figure 3b exhibits continuous and well-resolved lattice fringes, with *d*-spacing of ca. 0.27 nm corresponding to the 110 plane of STO.[57] Multidiffraction rings instead of dots are observedfrom the inset of Figure 3c, suggesting that the solvothermally synthesized STO possesses a polycrystalline nature. Figure 3c displays the morphology of Ag–STO nanocomposites where some dark spheres ranging in 10–20 nm were found dispersed on the top of STO surface. They are presumed to be Ag^0 nanoparticles due to the darker contrast. By taking high-resolution images on one sphere (Figure 3d), the average *d*-spacing value ca. 0.24 nm was determined, corresponding to the 111 plane of Ag.[58]

DOI: 10.1021/acsami.5b11887
ACS Appl. Mater. Interfaces 2016, 8, 4165–4174

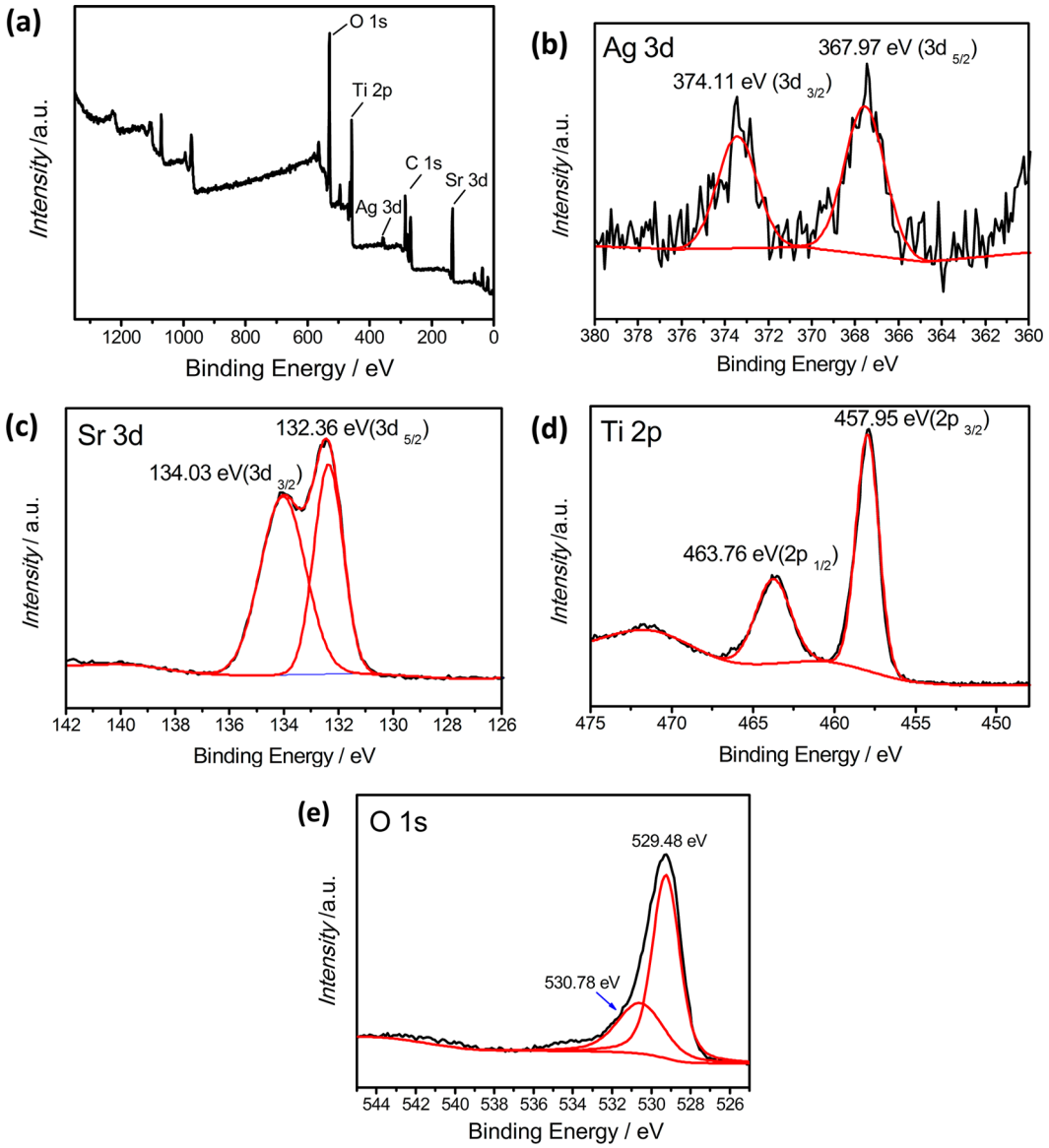

Figure 2. XPS spectra of the 0.5% Ag–$SrTiO_3$ nanocomposite: (a) survey spectrum; (b) Ag 3d; (c) Sr 3d; (d) Ti 2p and (e) O 1s.

Therefore, Ag nanoparticles modified STO nanocomposites were successfully synthesized via one-pot solvothermal method. Combined with the above characterization results, the formation mechanism of Ag–STO nanocomposites was proposed tentatively as illustrated in Scheme S1 (Supporting Information). The formation of STO mainly follows the "diffusion reaction" and "oriented attachment" processes,[59] in which the mineralizing agent NaOH plays an important role in forming STO and Ag nanocrystals. No STO was formed at NaOH concentration of 0.1 mol L^{-1} or below in our study. Therefore, it is postulated that high concentration of OH^- facilitates the hydrolysis of TTIP to form negative charged titanium sol, and attract positive charged Sr^{2+} ions to form $SrTiO_3$ nuclei. Moreover, Ag^+ could be quickly precipitated with OH^-, producing AgOH and further into Ag_2O and H_2O. In the presence of solvent ethanol, Ag_2O was reduced to Ag^0 under heated conditions. Unreacted Ag^+ and Ag_2O in the vessel can be further reduced to Ag^0 (for detailed reaction routes, see eqs 1–4).[60] Because $SrTiO_3$ and Ag are both crystallized in cubic structure with similar lattice spacing, they are more likely to be attached and achieve better lattice matching. Currently, the parameters influencing the particle size of Ag are unknown, whereas the loading amount of Ag could be easily tuned by changing the precursor concentration of Ag^+.

$$2Ag^+ + 2OH^- \rightarrow Ag_2O + H_2O \quad (1)$$

$$Ag_2O + C_2H_5OH \rightarrow 2Ag + CH_3CHO + H_2O \quad (2)$$

$$2Ag^+ + CH_3CHO + 2OH^- \rightarrow 2Ag + CH_3COOH + H_2O \quad (3)$$

$$Ag_2O + CH_3CHO \rightarrow 2Ag + CH_3COOH \quad (4)$$

3.3. Photocatalytic Performance, Selectivity and Stability. The photocatalytic activities of the bare STO, Ag–STO nanocomposites and commercial P25 were evaluated for the degradation of NO under visible irradiation ($\lambda > 420$ nm). The NO removal rates against irradiation time over different photocatalysts are plotted in Figure 4a. The dark adsorption differences over distinct photocatalysts were first excluded because they possess comparable surface area (see Table S1).

DOI: 10.1021/acsami.5b11887
ACS Appl. Mater. Interfaces 2016, 8, 4165–4174

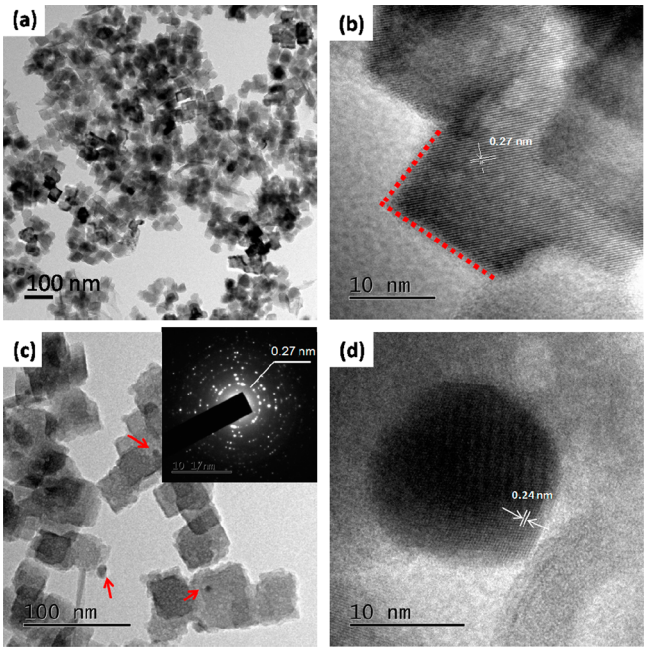

Figure 3. (a) Low-magnification TEM image of pristine STO; (b) high-resolution TEM image of pristine STO; (c) TEM image of 0.5% Ag−STO nanocomposite with arrows indicating Ag nanoparticles; inset is SAED image of pristine STO; and (d) HRTEM image of Ag nanoparticle on the top of STO surface.

As observed, pristine STO showed poorer photocatalytic performance for NO removal compared with P25, whereas coupling with Ag nanoparticles dramatically improved the photocatalytic efficiency. Although STO was inferior to P25 in terms of NO removal efficiency, it produced less toxic NO_2 molecules as we recorded (Figure 4b). According to the equation shown in section 2.3, the NO_2 selectivity of P25 was only 12.2%, which is twice that of STO (6.3%), suggesting that STO is more advantageous in realistic conditions. Previous studies showed that barium oxide (BaO) species could function as NO_x storage material to promote the photocatalytic activity of TiO_2.[35,61] Thus, it is assumed that Sr−O in STO matrix would have the similar behavior that promotes NO_x adsorption and avoids the release of NO_2.

Moreover, the effect of Ag loading ratio on photocatalytic efficiency was studied and shown in the curve. Among the four Ag−STO samples, 0.5% and 1% Ag−STO nanocomposites showed the best NO removal performances, with nearly 30% NO eliminated, which is twice that of pure STO. Further increase of Ag loading ratio to 1% only resulted in a marginal improvement in NO removal rate, suggesting that the optimal Ag loading ratio was around 0.5%. Presumably, the photocatalytic activity enhancement was mainly attributed to the LSPR effect of Ag nanoparticles, which leads to intense absorption in visible light region and contributes to the overall activity. With the increase of Ag loading amount, the LSPR effect becomes more significant and enhances removal rates of NO by transferring energy to STO. However, as more Ag nanoparticles were deposited on STO surface, photogenerated exciton population was increased, leading to an increased chance of charge recombination which might deteriorate the photocatalytic performance.[62] Therefore, 1% Ag−STO photocatalyst showed the similar performance with 0.5% Ag−STO on NO removal. Another important feature that is worth noting

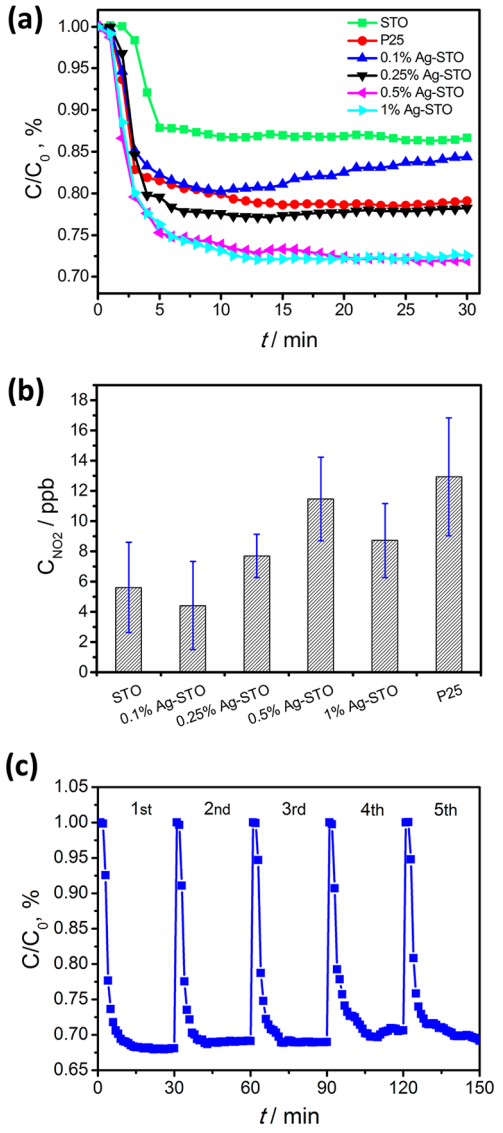

Figure 4. (a) Photocatalytic activity of Ag−STO, pristine STO and P25 samples as a function of irradiation time under visible light (λ > 420 nm), (b) NO_2 generation over Ag−STO, pristine STO and P25 samples, and (c) stability of 0.5% Ag−STO nanocomposites under visible light irradiation (λ > 420 nm).

is the increase of Ag loading ratio has negative impact on the selectivity, which is in other words, more NO_2 molecules are released over Ag−STO than pristine STO. This phenomenon can be ascribed to the occupancy of surface alkaline sites by Ag nanoparticles, which implies the importance of surface base property to promote NO_x conversion. Moreover, the repeated tests of 0.5% Ag−STO nanocomposite showed that the photocatalytic activity was largely maintained (Figure 4c), indicating the excellent stability of the synthesized nanocomposites.

3.4. Optical Properties. To gain an insight into the enhanced photocatalytic efficiency of Ag−STO nanocomposites for NO removal, optical characterizations were performed. The UV−vis absorbance spectra of Ag−STO nanocomposites were recorded, and the results are shown in Figure 5a. It is clearly observed that pristine STO harvested majority of light below 400 nm, and the calculated bandgap energy was 3.2 eV using the Kubelka−Munk function, which is in agreement with

DOI: 10.1021/acsami.5b11887
ACS Appl. Mater. Interfaces 2016, 8, 4165−4174

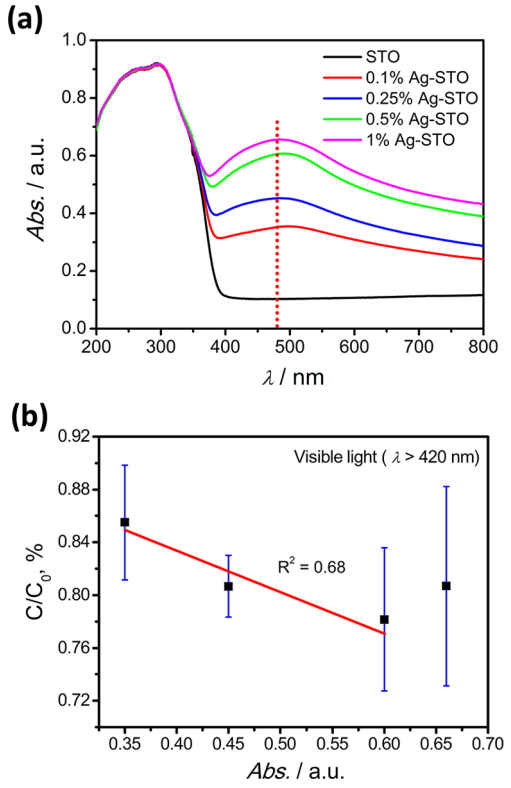

Figure 5. (a)UV−vis absorbance spectra of bare STO and Ag−STO nanocomposites at different Ag loading ratios, and (b) NO removal efficiency (C/C_0) against relative absorbance (a.u.) of Ag−STO nanocomposites.

previous results.[59] In addition, the Ag−STO nanocomposites displayed characteristic LSPR absorption in the range between 400 and 600 nm,[41] demonstrating the feasibility of the method to prepare plasmonic photocatalyst. The broadening of plasmon peaks, according to the literature, may be associated with the wide size distribution of Ag nanoparticles on STO surface.[41,63] Numbers of studies concluded that there is a positive correlation between SPR intensity and the photocatalytic efficiency improvement.[46,48,49] Through correlating C/C_0 with the SPR intensity (Figure 5b), we demonstrate that a quasi-linear relationship exists in the range of 0.1%−0.5% of Ag loading ratio. Whereas the further increase in sample absorbance does not lead to a continued growth in NO removal rate. This is probably due to other factors, such as the recombination of charge carriers in aggregated Ag nanoparticles becoming predominant at high loading ratios.

Essentially speaking, electron transfer, near-field electromagnetic and scattering are main mechanisms for LSPR promoted photocatalytic rate enhancement.[41,42] When semiconductor and plasmonic metal are in direct contact, as in our case, the electron transfer becomes the predominant mechanism.[44,64,65] Therefore, it is to say that the Ag LSPR induced the energetic electrons to inject to STO, like the dye-sensitized process, so that the electron concentration increased for the participation in chemical reactions. Scheme 1 shows the LSPR mediated charge transfer mechanism between Ag and STO. The flatband potential of STO relative to normal hydrogen electrode (NHE) was obtained from the Mott−Schottky plot (Figure S2) using the following equation:

$$\frac{1}{C^2} = \frac{1}{C_H{}^2} + \frac{2}{\varepsilon_r \varepsilon_0 q A^2 N_D}\left(U - U_{fb} - \frac{kT}{q}\right) \quad (5)$$

where C is the space charge layer capacitance, C_H is the Helmholtz double layer capacitance, and ε_r is the dielectric constant of the semiconductor, ε_0 is the permittivity of free space, q is electronic charge, A is electrode surface area, N_D is the doping density, U is the applied potential, U_{fb} is the flatband potential, k is the Bohr constant and T is the absolute temperature. For n-type semiconductor, the flatband potential is close to the conduction band position, therefore the conduction band position of STO is marked as −0.8 V vs Ag/AgCl in the NHE scale (at pH 7), and the valence band position is 2.4 V vs Ag/AgCl in the NHE scale (at pH 7). Because the work function of Ag is around 4.52−4.74 eV, the Fermi level of Ag lies somewhere between 0 and 0.2 V vs NHE. Energetic electrons will be formed with SPR excitation, which locate in the surface plasmon state 1.0−4.0 eV above the Fermi level. Such electronic state alignment allowed for the effective charge injection that contributed to the improved photocatalytic efficiency.

To probe the charge separation at the interface of Ag and STO, the photoluminescence (PL) spectra were recorded, and the results are shown in Figure 6. As observed, the pristine STO exhibited a broad PL signal in the range from 350 to 500 nm, with the obvious peak appearing at 400 nm attributed to the free exciton transition between band edges. The appearance of small peaks may indicate that there are binding exciton localized levels related to surface states on STO, which is in

Scheme 1. Mechanism of LSPR Induced Charge Injection from Ag Nanoparticles to STO on the NHE Scale

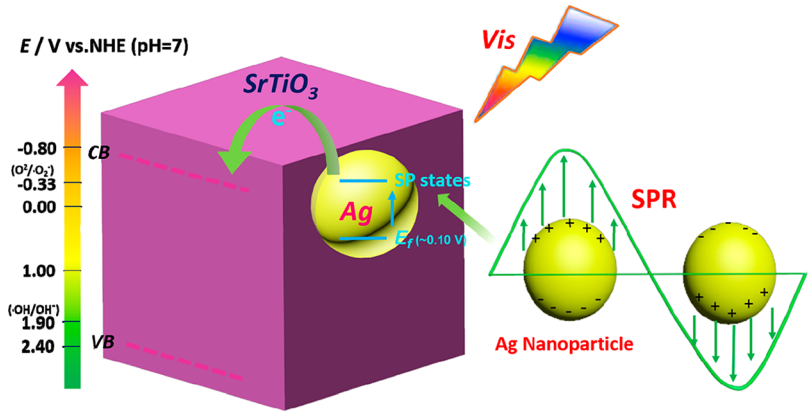

DOI: 10.1021/acsami.5b11887
ACS Appl. Mater. Interfaces 2016, 8, 4165−4174

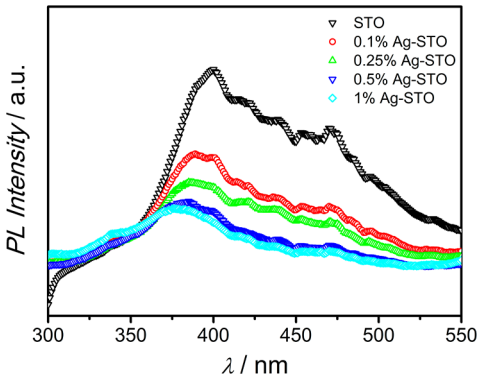

Figure 6. Photoluminescence spectra of bare STO and Ag–STO nanocomposites with laser excitation at 280 nm.

good agreement with the XPS results.[66] Another important feature is that the PL intensity in the vicinity of 400 nm declined pronouncedly after introducing Ag nanoparticles. It continues to decrease as the increase of Ag loading ratio from 0.1% to 0.5%. When the loading ratio further increased to 1%, the PL intensity decline became less significant. This trend is in accordance with the photocatalytic activity of samples. The results above indicate that Ag nanoparticles can effectively quench the charge carrier recombination at the interface, whereas at the high loading ratio (specifically at 1%) the quench effect becomes weaker, which may be due to the formation of aggregated Ag nanoparticles unfavorable for charge separation. Therefore, it is confirmed that the best photocatalytic activity of 0.5% Ag–STO is supported by the excellent visible light absorption arised from the LSPR effect and the enhanced charge separation across the interface.

3.5. Production of Reactive Radicals and Photocatalytic Reaction Mechanisms ESR Spectra. To probe the involvement of reactive oxygen species during photocatalytic removal of NO over STO and Ag–STO samples, the ESR technique was employed with DMPO as the spin trapping agent (shown in Figure 7). Keeping the suspension of photocatalysts in the dark showed no signals at all, indicating no radicals formed on both STO and Ag–STO samples in the absence of light. Under visible light irradiation, the obvious presence of sextet peaks with hyperfine splitting parameters of a_N = 1.43 mT and $a_{H\beta}$ = 1.17 mT, and the quartet peaks with hyperfine splitting parameters of $a_N = a_H$ = 1.49 mT are observed for 0.5% Ag–STO, suggesting the formation of DMPO–$\cdot O_2^-$ and DMPO–·OH adducts, whereas such signals are not detected over pristine STO exposed to visible irradiation.[67−69] Under UV light, both pristine STO and the 0.5% Ag–STO nanocomposite exhibited well-defined signals of DMPO–$\cdot O_2^-$ and DMPO–·OH adducts (see Figure S3). These results imply that coupling Ag nanoparticles with STO primarily induced the generation of reactive oxygen species upon visible light excitation. On the basis of previous discussion, the generated $\cdot O_2^-$ and ·OH radicals were essentially benefited from hot electron generation due to Ag plasmon resonance, and the depressed charge recombination across the Ag–STO interface. Therefore, the improved efficiency of photocatalytic NO removal over STO was essentially attributed to the significant generation of reactive oxygen species after coupling with plasmonic Ag nanoparticles.

Finally, the photocatalytic mechanism of NO reaction over Ag–STO nanocomposite was proposed based on aforementioned results and analyses. When Ag–STO is irradiated with light at the plasmon frequency of Ag nanoparticles, energetic electrons are produced and injected to the conduction band of STO by overcoming the Schottky barrier at the metal/semiconductor interface (reactions R1 and R2).[64] Part of these "hot" electrons have longer lifetime, being captured at surface Ti sites and reacting with adsorbed oxygen to produce $\cdot O_2^-$ and ·OH radicals (reactions R3–R5)).[70] To maintain electric neutrality, electrons on valence band of $SrTiO_3$ are transferred to Ag nanoparticles, leaving behind holes that can further react with surface hydroxyl group to produce ·OH radicals (reaction R6). Subsequently, the ·OH and $\cdot O_2^-$ radicals lead to the oxidation of NO to nitrate ions via different paths (reactions R7–R9).[7] FT-IR results confirmed the generation of nitrate ions after the photocatalytic reaction (see Figure S4). As a matter of fact, the photocatalytic activity would gradually decrease as the accumulation of nitrate ions on STO surface, but it can be easily restored by simply washing the photocatalyst with water.

$$\mathrm{Ag-NPs} + \lambda_{vis} \rightarrow \mathrm{Ag-NPs^*} \quad \text{(R1)}$$

$$\mathrm{Ag-NPs} + \mathrm{SrTiO_3} \rightarrow \mathrm{Ag-NPs^+} + \mathrm{SrTiO_3(e^-)} \quad \text{(R2)}$$

$$\mathrm{e^- + O_2 \rightarrow \cdot O_2^-} \quad \text{(R3)}$$

$$\mathrm{\cdot O_2^- + 2H^+ + e^- \rightarrow H_2O_2} \quad \text{(R4)}$$

$$\mathrm{H_2O_2 + e^- \rightarrow \cdot OH + OH^-} \quad \text{(R5)}$$

$$\mathrm{SrTiO_3(h^+) + OH^- \rightarrow \cdot OH} \quad \text{(R6)}$$

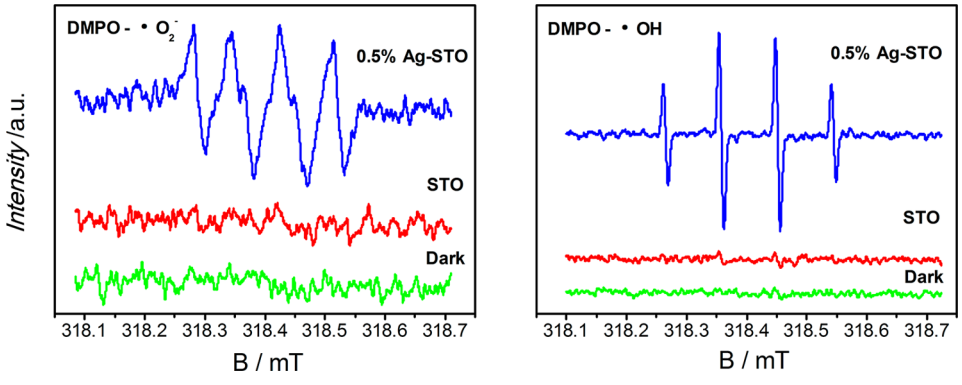

Figure 7. DMPO spin-trapping ESR spectra of STO and the 0.5% Ag–STO nanocomposite at visible wavelength of 420 nm, with light on for 10 min.

DOI: 10.1021/acsami.5b11887
ACS Appl. Mater. Interfaces 2016, 8, 4165–4174

$$NO + \cdot OH \rightarrow NO_2 + H_2O \quad (R7)$$

$$NO_2 + \cdot OH \rightarrow NO_3^- + H^+ \quad (R8)$$

$$NO + \cdot O_2^- \rightarrow NO_3^- \quad (R9)$$

4. CONCLUSIONS

In summary, a one-pot solvothermal approach for preparation of Ag−STO nanocomposites was proposed, and enhanced visible light activity for NO mitigation was achieved in this work. It was found that NaOH played a bifunctional role in promoting the growth of $SrTiO_3$ and Ag nanocrystallites. This method may be extended to fabricate other Ag−titanate (Ca, Ba) composite photocatalysts. Ag loading amount had an obvious effect on the photocatalytic efficiency for NO removal, with 0.5% Ag−STO exhibited the best performance among all samples. The improved photocatalytic activity was attributed to the enhanced visible light harvest derived from the plasmon resonance of Ag nanostructures, and reinforced charge separation at Ag−STO interface. The ESR studies suggested that both ·OH and $\cdot O_2^-$ radicals were involved in the photocatalytic oxidation of NO. Coupling Ag nanostructures with STO also led to the production of more radicals available for NO oxidation. Moreover, NO_2 generation over STO was mitigated comparing with P25, suggesting that the presence of alkaline sites may be beneficial for adsorption of intermediates. Presumably, crystal facet control over STO with more Sr−O termination might be favorable for NO adsorption, and this work is currently under investigation in our group. Finally, the specific reaction pathway of NO over STO needs in-depth investigation by, for example, the in situ FT-IR technique.

■ ASSOCIATED CONTENT

Supporting Information

The Supporting Information is available free of charge on the ACS Publications website at DOI: 10.1021/acsami.5b11887.

SEM images, BET results, Mott−Schottky plot, a schematic illustration of one-pot synthesis of Ag−STO nanocomposites, the ESR spectra of samples under UV light excitation and FT-IR spectra (PDF).

■ AUTHOR INFORMATION

Corresponding Authors

*Prof. Yu Huang. E-mail: huangyu@ieecas.cn.
*Prof. Jun-ji Cao. E-mail: cao@loess.llqg.ac.cn.

Notes

The authors declare no competing financial interest.

■ ACKNOWLEDGMENTS

This research was financially supported by the National Science Foundation of China (41401567, 41573138), and was also partially supported by Research Grants Council of Hong Kong (PolyU 152083/14E), the research grant of Early Career Scheme (ECS 809813) from the Research Grant Council, Hong Kong SAR Government, Dean's Research Fund-Early Career Researchers (04022), Research Equipment Grant (REG-2), and Internal Research Grant (R3429) from The Hong Kong Institute of Education.

■ REFERENCES

(1) Huang, R.-J.; Zhang, Y.; Bozzetti, C.; Ho, K.-F.; Cao, J.-J.; Han, Y.; Daellenbach, K. R.; Slowik, J. G.; Platt, S. M.; Canonaco, F.; Zotter, P.; Wolf, R.; Pieber, S. M.; Bruns, E. A.; Crippa, M.; Ciarelli, G.; Piazzalunga, A.; Schwikowski, M.; Abbaszade, G.; Schnelle-Kreis, J.; Zimmermann, R.; An, Z.; Szidat, S.; Baltensperger, U.; Haddad, I. E.; Prevot, A. S. H. High Secondary Aerosol Contribution to Particulate Pollution During Haze Events in China. *Nature* **2014**, *514*, 218−222.

(2) Gómez Alvarez, E.; Wortham, H.; Strekowski, R.; Zetzsch, C.; Gligorovski, S. Atmospheric Photosensitized Heterogeneous and Multiphase Reactions: From Outdoors to Indoors. *Environ. Sci. Technol.* **2012**, *46*, 1955−1963.

(3) Granger, P.; Parvulescu, V. I. Catalytic NO_x Abatement Systems for Mobile Sources: From Three-Way to Lean Burn after-Treatment Technologies. *Chem. Rev.* **2011**, *111*, 3155−3207.

(4) Hu, P.; Huang, Z.; Gu, X.; Xu, F.; Gao, J.; Wang, Y.; Chen, Y.; Tang, X. Alkali-Resistant Mechanism of a Hollandite $DeNO_x$ Catalyst. *Environ. Sci. Technol.* **2015**, *49*, 7042−7047.

(5) Joicy, S.; Saravanan, R.; Prabhu, D.; Ponpandian, N.; Thangadurai, P. Mn^{2+} ion Influenced Optical and Photocatalytic Behaviour of Mn-ZnS Quantum Dots Prepared by a Microwave Assisted Technique. *RSC Adv.* **2014**, *4*, 44592−44599.

(6) Carey, J. H.; Lawrence, J.; Tosine, H. M. Photodechlorination of PCB's in the Presence of Titanium Dioxide in Aqueous Suspensions. *Bull. Environ. Contam. Toxicol.* **1976**, *16*, 697−701.

(7) Sugrañez, R.; Balbuena, J.; Cruz-Yusta, M.; Martín, F.; Morales, J.; Sánchez, L. Efficient Behaviour of Hematite Towards the Photocatalytic Degradation of NO_x Gases. *Appl. Catal., B* **2015**, *165*, 529−536.

(8) Sofianou, M. V.; Tassi, M.; Psycharis, V.; Boukos, N.; Thanos, S.; Vaimakis, T.; Yu, J.; Trapalis, C. Solvothermal Synthesis and Photocatalytic Performance of Mn^{4+}-doped Anatase Nanoplates with Exposed {001} Facets. *Appl. Catal., B* **2015**, *162*, 27−33.

(9) Ai, Z.; Ho, W.; Lee, S.; Zhang, L. Efficient Photocatalytic Removal of NO in Indoor Air with Hierarchical Bismuth Oxybromide Nanoplate Microspheres under Visible Light. *Environ. Sci. Technol.* **2009**, *43*, 4143−4150.

(10) Ai, Z.; Ho, W.; Lee, S. Efficient Visible Light Photocatalytic Removal of NO with BiOBr-Graphene Nanocomposites. *J. Phys. Chem. C* **2011**, *115*, 25330−25337.

(11) Ho, W.; Zhang, Z.; Xu, M.; Zhang, X.; Wang, X.; Huang, Y. Enhanced Visible Light Driven Photocatalytic Removal of NO: Effect on Layer Distortion on g-C_3N_4 by H_2 Heating. *Appl. Catal., B* **2015**, *179*, 106−112.

(12) Ho, W.; Zhang, Z.; Lin, W.; Huang, S.; Zhang, X.; Wang, X.; Huang, Y. Copolymerization with 2,4,6-Triaminopyrimidine for the Rolling-up the Layer Structure, Tunable Electronic Properties, and Photocatalysis of g-C_3N_4. *ACS Appl. Mater. Interfaces* **2015**, *7*, 5497−5505.

(13) Ge, S.; Zhang, L. Efficient Visible Light Driven Photocatalytic Removal of RhB and NO with Low Temperature Synthesized $In(OH)_xS_y$ Hollow Nanocubes: A Comparative Study. *Environ. Sci. Technol.* **2011**, *45*, 3027−3033.

(14) Su, C.; Ran, X.; Hu, J.; Shao, C. Photocatalytic Process of Simultaneous Desulfurization and Denitrification of Flue Gas by TiO_2-Polyacrylonitrile Nanofibers. *Environ. Sci. Technol.* **2013**, *47*, 11562−11568.

(15) Wu, J. C. S.; Cheng, Y.-T. In Situ FTIR Study of Photocatalytic NO Reaction on Photocatalysts under UV Irradiation. *J. Catal.* **2006**, *237*, 393−404.

(16) Gandolfo, A.; Bartolomei, V.; Gomez Alvarez, E.; Tlili, S.; Gligorovski, S.; Kleffmann, J.; Wortham, H. The Effectiveness of Indoor Photocatalytic Paints on NO_x and HONO Levels. *Appl. Catal., B* **2015**, *166−167*, 84−90.

(17) Wu, Q.; van de Krol, R. Selective Photoreduction of Nitric Oxide to Nitrogen by Nanostructured TiO_2 Photocatalysts: Role of Oxygen Vacancies and Iron Dopant. *J. Am. Chem. Soc.* **2012**, *134*, 9369−9375.

(18) Dong, F.; Wang, Z.; Li, Y.; Ho, W.-K.; Lee, S. C. Immobilization of Polymeric g-C_3N_4 on Structured Ceramic Foam for Efficient Visible Light Photocatalytic Air Purification with Real Indoor Illumination. *Environ. Sci. Technol.* **2014**, *48*, 10345−10353.

DOI: 10.1021/acsami.5b11887
ACS Appl. Mater. Interfaces 2016, 8, 4165−4174

(19) Negishi, N.; Matsuzawa, S.; Takeuchi, K.; Pichat, P. Transparent Micrometer-Thick TiO_2 Films on SiO_2-Coated Glass Prepared by Repeated Dip-Coating/Calcination: Characteristics and Photocatalytic Activities for Removing Acetaldehyde or Toluene in Air. *Chem. Mater.* **2007**, *19*, 3808−3814.
(20) Huang, Y.; Ai, Z.; Ho, W.; Chen, M.; Lee, S. Ultrasonic Spray Pyrolysis Synthesis of Porous Bi_2WO_6 Microspheres and Their Visible-Light-Induced Photocatalytic Removal of NO. *J. Phys. Chem. C* **2010**, *114*, 6342−6349.
(21) Folli, A.; Strøm, M.; Madsen, T. P.; Henriksen, T.; Lang, J.; Emenius, J.; Klevebrant, T.; Nilsson, Å. Field Study of Air Purifying Paving Elements Containing TiO_2. *Atmos. Environ.* **2015**, *107*, 44−51.
(22) Ballari, M. M.; Brouwers, H. J. H. Full Scale Demonstration of Air Purifying Pavement. *J. Hazard. Mater.* **2013**, *254*−*255*, 406−414.
(23) Gallus, M.; Akylas, V.; Barmpas, F.; Beeldens, A.; Boonen, E.; Boréave, A.; Cazaunau, M.; Chen, H.; Daële, V.; Doussin, J. F. Photocatalytic De-pollution in the Leopold II Tunnel in Brussels: NO_x Abatement Results. *Build. Environ.* **2015**, *84*, 125−133.
(24) Zhu, J.; Li, H.; Zhong, L.; Xiao, P.; Xu, X.; Yang, X.; Zhao, Z.; Li, J. Perovskite Oxides: Preparation, Characterizations, and Applications in Heterogeneous Catalysis. *ACS Catal.* **2014**, *4*, 2917−2940.
(25) Libby, W. F. Promising Catalyst for Auto Exhaust. *Science* **1971**, *171*, 499−500.
(26) Roy, S.; Hegde, M. S.; Madras, G. Catalysis for NO_x Abatement. *Appl. Energy* **2009**, *86*, 2283−2297.
(27) Chen, H. C.; Huang, C. W.; Wu, J. C. S.; Lin, S. T. Theoretical Investigation of the Metal-Doped $SrTiO_3$ Photocatalysts for Water Splitting. *J. Phys. Chem. C* **2012**, *116*, 7897−7903.
(28) Cho, S.; Jang, J. W.; Zhang, W.; Suwardi, A.; Wang, H.; Wang, D.; Macmanus-Driscoll, J. L. Single-Crystalline Thin Films for Studying Intrinsic Properties of $BiFeO_3$-$SrTiO_3$ Solid Solution Photoelectrodes in Solar Energy Conversion. *Chem. Mater.* **2015**, *27*, 6635−6641.
(29) Iwashina, K.; Kudo, A. Rh-Doped $SrTiO_3$ Photocatalyst Electrode Showing Cathodic Photocurrent for Water Splitting under Visible Light Irradiation. *J. Am. Chem. Soc.* **2011**, *133*, 13272−13275.
(30) Tan, H.; Zhao, Z.; Zhu, W.-b.; Coker, E. N.; Li, B.; Zheng, M.; Yu, W.; Fan, H.; Sun, Z. Oxygen Vacancy Enhanced Photocatalytic Activity of Pervoskite $SrTiO_3$. *ACS Appl. Mater. Interfaces* **2014**, *6*, 19184−19190.
(31) Ouyang, S.; Tong, H.; Umezawa, N.; Cao, J.; Li, P.; Bi, Y.; Zhang, Y.; Ye, J. Surface Alkalinization Induced Enhancement of Photocatalytic H_2 Evolution over $SrTiO_3$ Based Photocatalysts. *J. Am. Chem. Soc.* **2012**, *134*, 1974−1977.
(32) Wang, D.; Kako, T.; Ye, J. New Series of Solid-Solution Semiconductors $(AgNbO_3)_{1-x}(SrTiO_3)_x$ with Modulated Band Structure and Enhanced Visible Light Photocatalytic Activity. *J. Phys. Chem. C* **2009**, *113*, 3785−3792.
(33) Wrighton, M. S.; Ellis, A. B.; Wolczanski, P. T.; Morse, D. L.; Abrahamson, H. B.; Ginley, D. S. Strontium titanate photoelectrodes. Efficient Photoassisted Electrolysis of Water at Zero Applied Potential. *J. Am. Chem. Soc.* **1976**, *98*, 2774−2779.
(34) Burnside, S.; Moser, J.-E.; Brooks, K.; Grätzel, M.; Cahen, D. Nanocrystalline Mesoporous Strontium Titanate as Photoelectrode Material for Photosensitized Solar Devices: Increasing Photovoltage through Flatband Potential Engineering. *J. Phys. Chem. B* **1999**, *103*, 9328−9332.
(35) Yamamoto, A.; Mizuno, Y.; Teramura, K.; Hosokawa, S.; Tanaka, T. Surface Ba Species Effective for Photoassisted NO_x Storage Over Ba-Modified TiO_2 Photocatalysts. *Appl. Catal., B* **2016**, *180*, 283−290.
(36) Li, H.; Yin, S.; Wang, Y.; Sekino, T.; Lee, S. W.; Sato, T. Roles of Cr^{3+} Doping and Oxygen Vacancies in $SrTiO_3$ Photocatalysts with High Visible Light Activity for NO Removal. *J. Catal.* **2013**, *297*, 65−69.
(37) Sulaeman, U.; Yin, S.; Sato, T. Solvothermal Synthesis and Photocatalytic Properties of Chromium-Doped $SrTiO_3$ Nanoparticles. *Appl. Catal., B* **2011**, *105*, 206−210.
(38) Wang, Q.; Hisatomi, T.; Ma, S. S. K.; Li, Y.; Domen, K. Core/Shell Structured La- and Rh-Codoped $SrTiO_3$ as a Hydrogen Evolution Photocatalyst in Z-Scheme Overall Water Splitting under Visible Light Irradiation. *Chem. Mater.* **2014**, *26*, 4144−4150.
(39) Modak, B.; Ghosh, S. K. Role of F in Improving Photocatalytic Activity of Rh-Doped $SrTiO_3$. *J. Phys. Chem. C* **2015**, *119*, 7215−7224.
(40) Saravanan, R.; Mansoob, K. M.; Gupta, V. K.; Mosquera, E.; Gracia, F.; Narayanan, V.; Stephen, A. ZnO/Ag/CdO Nanocomposite for Visible Light Induced Photocatalytic Degradation of Industrial Textile Effluents. *J. Colloid Interface Sci.* **2015**, *452*, 126−133.
(41) Linic, S.; Christopher, P.; Ingram, D. B. Plasmonic-Metal Nanostructures for Efficient Conversion of Solar to Chemical Energy. *Nat. Mater.* **2011**, *10*, 911−921.
(42) Hou, W.; Cronin, S. B. A Review of Surface Plasmon Resonance-Enhanced Photocatalysis. *Adv. Funct. Mater.* **2013**, *23*, 1612−1619.
(43) Wang, P.; Huang, B.; Dai, Y.; Whangbo, M. H. Plasmonic Photocatalysts: Harvesting Visible Light with Noble Metal Nanoparticles. *Phys. Chem. Chem. Phys.* **2012**, *14*, 9813−9825.
(44) Tian, Y.; Tatsuma, T. Plasmon-Induced Photoelectrochemistry at Metal Nanoparticles Supported on Nanoporous TiO_2. *Chem. Commun.* **2004**, *16*, 1810−1811.
(45) Furube, A.; Du, L.; Hara, K.; Katoh, R.; Tachiya, M. Ultrafast Plasmon-Induced Electron Transfer from Gold Nanodots into TiO_2 Nanoparticles. *J. Am. Chem. Soc.* **2007**, *129*, 14852−14853.
(46) Amrollahi, R.; Hamdy, M. S.; Mul, G. Understanding Promotion of Photocatalytic Activity of TiO_2 by Au Nanoparticles. *J. Catal.* **2014**, *319*, 194−199.
(47) Hou, W.; Liu, Z.; Pavaskar, P.; Hung, W. H.; Cronin, S. B. Plasmonic enhancement of photocatalytic decomposition of methyl orange under visible light. *J. Catal.* **2011**, *277*, 149−153.
(48) He, Y.; Basnet, P.; Murph, S. E. H.; Zhao, Y. Ag Nanoparticle Embedded TiO_2 Composite Nanorod Arrays Fabricated by Oblique Angle Deposition: Toward Plasmonic Photocatalysis. *ACS Appl. Mater. Interfaces* **2013**, *5*, 11818−11827.
(49) Ding, D.; Liu, K.; He, S.; Gao, C.; Yin, Y. Ligand-Exchange Assisted Formation of Au/TiO_2 Schottky Contact for Visible-Light Photocatalysis. *Nano Lett.* **2014**, *14*, 6731−6736.
(50) Ai, Z.; Ho, W.; Lee, S.; Zhang, L. Efficient Photocatalytic Removal of NO in Indoor Air with Hierarchical Bismuth Oxybromide Nanoplate Microspheres under Visible Light. *Environ. Sci. Technol.* **2009**, *43*, 4143−4150.
(51) Ma, J.; He, H.; Liu, F. Effect of Fe on the Photocatalytic Removal of NO_x Over Visible Light Responsive Fe/TiO_2 Catalysts. *Appl. Catal., B* **2015**, *179*, 21−28.
(52) Sharma, D.; Upadhyay, S.; Satsangi, V. R.; Shrivastav, R.; Waghmare, U. V.; Dass, S. Improved Photoelectrochemical Water Splitting Performance of Cu_2O/$SrTiO_3$ Heterojunction Photoelectrode. *J. Phys. Chem. C* **2014**, *118*, 25320−25329.
(53) Langford, J. I.; Wilson, A. J. C.; Scherrer After. Sixty Years: A Survey and Some New Results in the Determination of Crystallite Size. *J. Appl. Crystallogr.* **1978**, *11*, 102−113.
(54) Yang, J.; Zhang, F.; Chen, Y.; Qian, S.; Hu, P.; Li, W.; Deng, Y.; Fang, Y.; Han, L.; Luqman, M.; Zhao, D. Core-Shell Ag@SiO_2@mSiO_2 Mesoporous Nanocarriers for Metal-Enhanced Fluorescence. *Chem. Commun.* **2011**, *47*, 11618−11620.
(55) NIST. X-ray Photoelectron Spectroscopy Database, Version 4.1; National Institute of Standards and Technology: Gaithersburg, 2012; http://srdata.nist.gov/xps/.
(56) Zhang, Q.; Wang, L.; Feng, J.; Xu, H.; Yan, W. Enhanced Photoelectrochemical Performance by Synthesizing CdS Decorated Reduced TiO_2 Nanotube Arrays. *Phys. Chem. Chem. Phys.* **2014**, *16*, 23431−23439.
(57) Ouyang, S.; Li, P.; Xu, H.; Tong, H.; Liu, L.; Ye, J. Bifunctional-Nanotemplate Assisted Synthesis of Nanoporous $SrTiO_3$ Photocatalysts Toward Efficient Degradation of Organic Pollutant. *ACS Appl. Mater. Interfaces* **2014**, *6*, 22726−22732.
(58) Shi, H.; Chen, J.; Li, G.; Nie, X.; Zhao, H.; Wong, P.-K.; An, T. Synthesis and Characterization of Novel Plasmonic Ag/AgX-CNTs (X

DOI: 10.1021/acsami.5b11887
ACS Appl. Mater. Interfaces 2016, 8, 4165−4174

= Cl, Br, I) Nanocomposite Photocatalysts and Synergetic Degradation of Organic Pollutant under Visible Light. *ACS Appl. Mater. Interfaces* **2013**, *5*, 6959−6967.
(59) Zhan, H.; Chen, Z.-G.; Zhuang, J.; Yang, X.; Wu, Q.; Jiang, X.; Liang, C.; Wu, M.; Zou, J. Correlation between Multiple Growth Stages and Photocatalysis of $SrTiO_3$ Nanocrystals. *J. Phys. Chem. C* **2015**, *119*, 3530−3537.
(60) Pan, J.; Sun, Y.; Wang, Z.; Wan, P.; Liu, X.; Fan, M. Nano Silver Oxide (AgO) as a Super High Charge/Discharge Rate Cathode Material for Rechargeable Akaline Batteries. *J. Mater. Chem.* **2007**, *17*, 4820−4825.
(61) Yamamoto, A.; Mizuno, Y.; Teramura, K.; Hosokawa, S.; Tanaka, T. Noble-Metal-Free NO_x Storage over Ba-Modified TiO_2 Photocatalysts under UV-Light Irradiation at Low Temperatures. *ACS Catal.* **2015**, *5*, 2939−2943.
(62) Du, P.; Jing, P.; Li, D.; Cao, Y.; Liu, Z.; Sun, Z. Plasmonic Ag@ Oxide Nanoprisms for Enhanced Performance of Organic Solar Cells. *Small* **2015**, *11*, 2454−2462.
(63) Gao, C.; Hu, Y.; Wang, M.; Chi, M.; Yin, Y. Fully Alloyed Ag/ Au Nanospheres: Combining the Plasmonic Property of Ag with the Stability of Au. *J. Am. Chem. Soc.* **2014**, *136*, 7474−7479.
(64) Yu, J.; Dai, G.; Huang, B. Fabrication and Characterization of Visible-Light-Driven Plasmonic Photocatalyst $Ag/AgCl/TiO_2$ Nanotube Arrays. *J. Phys. Chem. C* **2009**, *113*, 16394−16401.
(65) Shi, H.; Chen, J.; Li, G.; Nie, X.; Zhao, H.; Wong, P. K.; An, T. Synthesis and Characterization of Novel Plasmonic Ag/AgX-CNTs (X = Cl, Br, I) Nanocomposite Photocatalysts and Synergetic Degradation of Organic Pollutant under Visible Light. *ACS Appl. Mater. Interfaces* **2013**, *5*, 6959−6967.
(66) Zhang, W. F.; Zhang, M. S.; Yin, Z.; Chen, Q. Photoluminescence in Anatase Titanium Dioxide Nanocrystals. *Appl. Phys. B: Lasers Opt.* **2000**, *70*, 261−265.
(67) He, W.; Wu, H.; Wamer, W. G.; Kim, H. K.; Zheng, J.; Jia, H.; Zheng, Z.; Yin, J. J. Unraveling the Enhanced Photocatalytic Activity and Phototoxicity of ZnO/Metal Hybrid Nanostructures from Generation of Reactive Oxygen Species and Charge Carriers. *ACS Appl. Mater. Interfaces* **2014**, *6*, 15527−15535.
(68) Wang, Z.; Ma, W.; Chen, C.; Ji, H.; Zhao, J. Probing Paramagnetic Species in Titania-Based Heterogeneous Photocatalysis by Electron Spin Resonance (ESR) Spectroscopy-A Mini Review. *Chem. Eng. J.* **2011**, *170*, 353−362.
(69) Zhao, W.; Ma, W.; Chen, C.; Zhao, J.; Shuai, Z. Efficient Degradation Of Toxic Organic Pollutants With Ni_2O_3/TiO_2-Xbx Under Visible Irradiation. *J. Am. Chem. Soc.* **2004**, *126*, 4782−4783.
(70) Amidani, L.; Naldoni, A.; Malvestuto, M.; Marelli, M.; Glatzel, P.; Dal Santo, V.; Boscherini, F. Probing Long-Lived Plasmonic-Generated Charges in TiO_2/Au by High-Resolution X-ray Absorption Spectroscopy. *Angew. Chem.* **2015**, *127*, 5503−5506.

DOI: 10.1021/acsami.5b11887
ACS Appl. Mater. Interfaces 2016, 8, 4165−4174